Research Article Vol. 10, No. 3 / March 2023 / Optica 349

Platform-agnostic waveguide integration of high-speed photodetectors with evaporated tellurium thin films

Geun Ho Ahn,[1,*,†] Alexander D. White,[1,5,†] Hyungjin Kim,[2,†] Naoki Higashitarumizu,[3,4] Felix M. Mayor,[1] Jason F. Herrmann,[1] Wentao Jiang,[1] Kevin K. S. Multani,[1] Amir H. Safavi-Naeini,[1] Ali Javey,[3,4] and Jelena Vučković[1]

[1]E. L. Ginzton Laboratory, Stanford University, Stanford, California 94305, USA
[2]Department of Materials Science and Engineering, Yonsei University, Seoul 03722, Republic of Korea
[3]Department of Electrical Engineering and Computer Sciences, University of California, Berkeley, California 94720, USA
[4]Materials Sciences Division, Lawrence Berkeley National Laboratory, Berkeley, California 94720, USA
[5]e-mail: adwhite@stanford.edu
*gahn@stanford.edu

Received 9 September 2022; revised 9 January 2023; accepted 24 January 2023; published 1 March 2023

Many attractive photonics platforms still lack integrated photodetectors due to inherent material incompatibilities and lack of process scalability, preventing their widespread deployment. Here, we address the problem of scalably integrating photodetectors in a photonics-platform-independent manner. Using a thermal evaporation and deposition technique developed for nanoelectronics, we show that tellurium, a quasi-2D semi-conductive element, can be evaporated at low temperatures directly onto photonic chips to form air-stable, high-speed, ultrawide-band photodetectors. We demonstrate detection from visible (520 nm) to short-wave infrared (2.4 μm), a bandwidth of more than 40 GHz, and platform-independent scalable integration with photonic structures in silicon, silicon nitride, and lithium niobate.

https://doi.org/10.1364/OPTICA.475387

1. INTRODUCTION

Upcoming applications in nonlinear and quantum photonics have led to the proliferation of alternative material platforms that offer wider transparency windows, lower loss, and a diversity of optical nonlinearities [1–6]. Applications of these platforms include mid-infrared (IR) circuits for environment sensing and communication, nonlinear optics for frequency conversion and generation and metrology, and ultra-high-speed data encoding. Integrated photodetectors play a critical role in these technologies, serving as the primary readout for many systems [7,8]. However, a vast majority of novel photonics material platforms do not have easily integratable photodetectors, and instead rely on external detection. This lack of on-chip photodetection prevents the scaling and deployment of many photonic integrated circuits (PIC).

Current approaches to on-chip photodetection are either platform dependent or challenging to scale. For instance, traditional photodiode materials such as germanium and III-V require stringent material synthesis processing such as high synthesis temperatures and crystal lattice matching to their host material [9–11], and are therefore limited to operation on silicon on insulator (SOI) or III-V platforms. Recent work depositing these materials in amorphous form is a promising avenue towards platform independence, but the reduced carrier mobility in amorphous material necessitates nano-scale fabrication features [12]. Two-dimensional (2D) materials, many of which are photo-active [13–19], have no such requirement of crystal lattice matching requirement owing to their naturally terminated surface, and can be transferred to nearly any substrate [20–22]. However, manufacturing, stability, and scaling remain as significant obstacles for the practicality of 2D photodetector integration [23,24]. The mechanical exfoliation process used to make 2D based photodetectors is currently a stochastic, labor-intensive manual process, and while there are constant advancements in large-area synthesis of 2D materials [25], there are still many outstanding challenges, including small grain size, strain, and reliable material transfer [23].

Here, we show that thin film tellurium (Te) can be lithographically defined and evaporated at low temperatures directly onto photonic structures to form easy-to-fabricate functional photodetectors. We utilize a thermal evaporation and deposition technique developed for nanoelectronics that forms a crystalline quasi-2D structure with extremely high carrier mobility [26–28]. The scalability of thermal evaporation and lithographic definition of active material allows us to demonstrate an array of 64 functional detectors fabricated in parallel. Additionally, the high mobility of the evaporated Te allows us to demonstrate state-of-the-art device bandwidths of over 40 GHz. These detectors can be fabricated on a variety of novel PIC platforms (here, we show silicon, silicon

nitride, and lithium niobate), and the small bandgap of the evaporated Te allows operation from visible to mid-IR. Under low-power and low-frequency optical excitations, avalanche gain allows us to reach responsivities up to 1.9 AW^{-1} at 520 nm, 0.8 AW^{-1} at 1550 nm, and 0.15 AW^{-1} at 2360 nm. We find that the evaporated Te is air stable, with no significant degradation in devices left in air for over a one month period, corroborating observations in flakes [19]. Finally, we show that because we can integrate these photodetectors directly on top of photonic structures, we can use integrated devices such as micro-resonators to enhance the absorption of the detector and reduce the relative dark current.

2. RESULTS

Simple lithographic fabrication of Te photodetectors would allow for interfacing with photonics platforms that lack photodection including mid-IR silicon circuits, nonlinear photonics in silicon nitride, and ultra-high-speed modulators in lithium niobate [Fig. 1(a)]. As shown schematically in Fig. 1(b), the fabrication process for Te photodetectors is scalable and straightforward. We first define waveguide structures on an integrated photonics platform. To ensure even deposition onto the waveguide structure, we clad the waveguides with oxide; here, we achieve this by spinning on and annealing diluted H-SiOx (HSQ) liquid glass. We then lithographically define and deposit through evaporation the gold connections, Te photoconductor thin film, and palladium (Pd) contacts [Figs. 1(a)–1(c)]. The as-deposited Te thin films are poly-crystalline, as shown in Supplement 1 Fig. S1, and optical images of patterned Te thin films after liftoff on the PIC are shown in Supplement 1 Fig. S2. The Pd contacts are chosen for relatively low contact resistance to the Te [29], allowing the photodetector to operate in photoconductive mode. However, asymmetric contacts and other choices of metals such as Pd and Cr can allow for Schottky diode connections for lower dark currents [29]. By modulating the thickness of the Te layer, a large range of optical bandgaps is accessible, allowing for detection from the visible to mid-IR (up to 4.1 μm) [26]. Though the thickness of the Te layers used is extremely subwavelength, due to the proximity of the waveguide, nearly all of the light can be absorbed in just a few μm of propagation length, as shown by the length-dependent transmission measurement of Te films shown in Supplement 1 Fig. S3. The combination of low-temperature evaporation onto oxide and controllable bandgap allows for easy fabrication on top of nearly any integrated photonics platform for use with any wavelength, without damaging photonic, metal, or active structures already fabricated.

To test the scalability and reliability of this integration of Te photodetector scheme, we deposit in parallel a 64 element array of Te photodetectors on a silicon nitride PIC [Fig. 2(a)]. Here, each column of eight devices is fed by an underlying circuit that

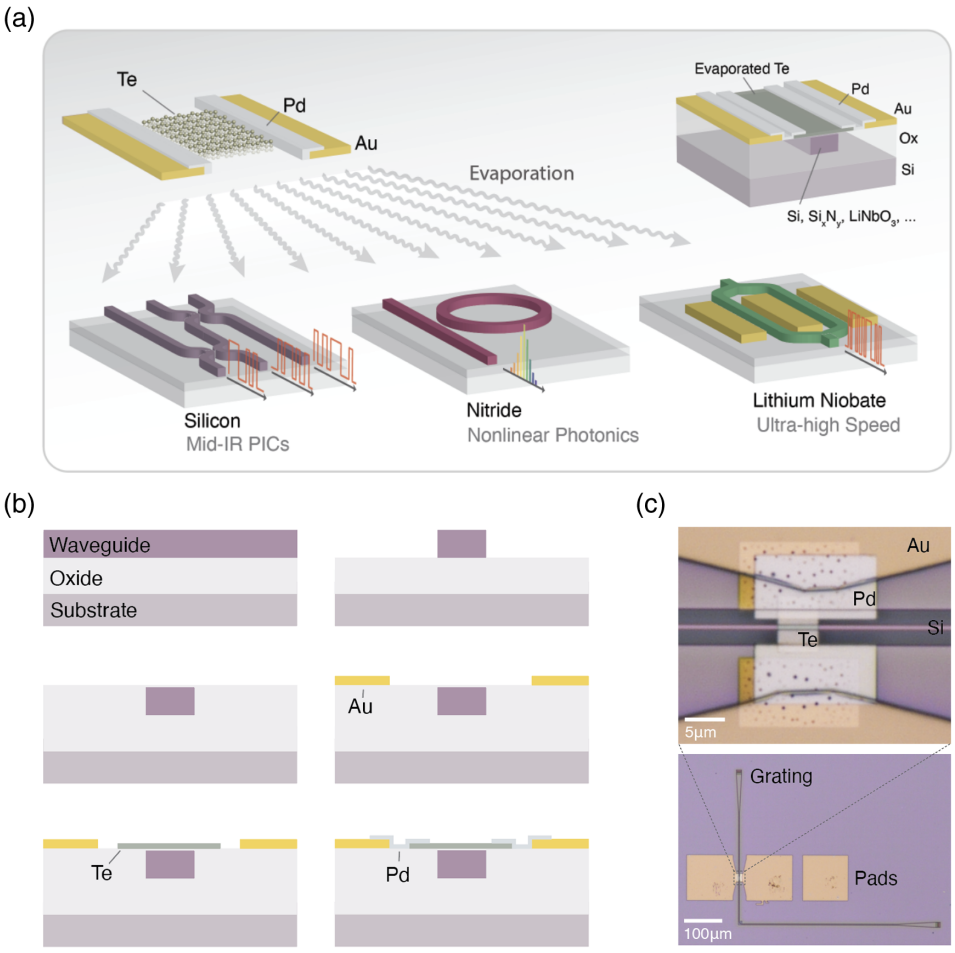

Fig. 1. Tellurium photodetectors. (a) Schematic of device. (b) Fabrication process flow. SOI or any other photonics platform is etched to form waveguides. HSQ liquid glass is used to fill gaps and smooth the top surface. Gold pads, tellurium devices, and finally palladium contacts are lithographically defined and evaporated. (c) Optical micrographs of a tellurium device (top) and its connection to waveguides and electronics (bottom).

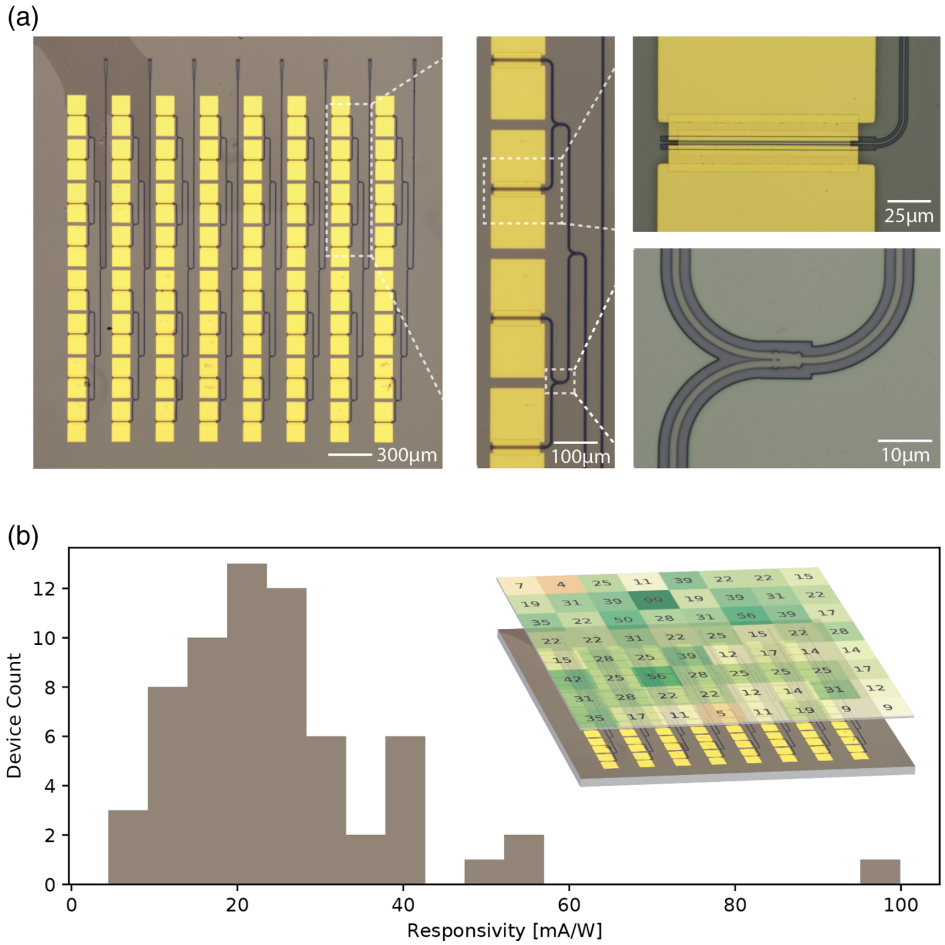

Fig. 2. Detector array. (a) Optical micrographs of 8 × 8 device array of Te photodetectors on silicon nitride. Each column of devices is fed optically by a grating coupler and splitter tree. (b) Histogram and mapping of device responsivity measured with 2 μW of 1550 nm optical power at 10 MHz.

splits light incident on a grating coupler into eight photodetector waveguides. By sending modulated light through the gratings, we can measure the responsivity of every device, as shown in Fig. 2(b). We find that every device in the array shows a measurable photoresponse, with a distribution centered around 25 $\mathrm{mAW^{-1}}$, corresponding to a 2% quantum efficiency. Through transfer length measurement (TLM) of Te films, we find that the devices have a contact resistance of approximately 250Ω, as shown in Supplement 1 Fig. S4. As the responsivity of these devices is measured at 10 MHz, there is minimal flicker (1/f) noise contribution, and the noise current can be approximated by the sum of thermal Johnson noise and shot noise [30]. By measuring the resistance, 27kΩ, and dark current, 114 μA, of a representative Te photodetector device, we estimate the noise equivalent power (NEP) to be 244 $\mathrm{pW}/\sqrt{\mathrm{Hz}}$.

We next measure both 8 and 16 nm thick Te on silicon to study the effect of carrier mobility. While 8 and 16 nm Te can both absorb 1550 nm light, the carrier mobility in 16 nm is significantly higher. While using thicker devices would increase mobility even further, this would also reduce the bandgap and thus increase the dark current due to absorption of thermal photons. We first verify the functionality of the devices by measuring the bias-voltage-dependent responsivity, shown in Figs. 3(a) and 3(b). We observe that the responsivity increases at very low optical power and frequency as shown in Figs. 3(c) and 3(d). This is likely due to avalanching of carriers trapped at defect sites [31]. As the carrier regeneration at these defects is a slow process, this limits the gain at higher input powers and higher frequencies. We see a maximum responsivity of 0.8 $\mathrm{AW^{-1}}$. At higher optical power levels and frequencies much larger than those at which we see gain, the responsivity is extremely uniform, as shown in Fig. 3(e), with 6 $\mathrm{mAW^{-1}}$ at 8 nm and 11 $\mathrm{mAW^{-1}}$ at 16 nm. At these frequencies and power levels, we see that the nonlinearity of the photoresponse is significantly reduced (shown in Supplement 1 Fig. S5). We see that, due to the lower carrier mobility with thinner Te [27], the frequency response of the 8 nm devices rolls off with a 3 dB bandwidth near 2 GHz, while the 16 nm devices show no degradation in responsivity out to at least 22 GHz, where our measurements were limited. From the roll-off frequency, we can estimate the transit time present in the device as defined by $\tau_{tr} = l^2/2\mu V_d$, where μ is the carrier mobility, and l is the separation length between electrodes. For the Te photodetectors presented here, we use $l = 3 \times 10^{-6}$ m for ease of fabrication. From the measurements, we estimate a mobility of 45 $\mathrm{cm^2V^{-1}s^{-1}}$ for 8 nm Te, and a mobility of more than 250 $\mathrm{cm^2V^{-1}s^{-1}}$ for 16 nm Te, which is in good agreement with previous reports on the experimental measurements of Te with the corresponding thicknesses [27]. In addition, the waveguide integrated Te photodetectors show excellent stability, as shown by measurements taken 1.5 months apart (Supplement 1 Fig. S6). Within this time period, the Te photodetectors were left in the air and did not show noticeably

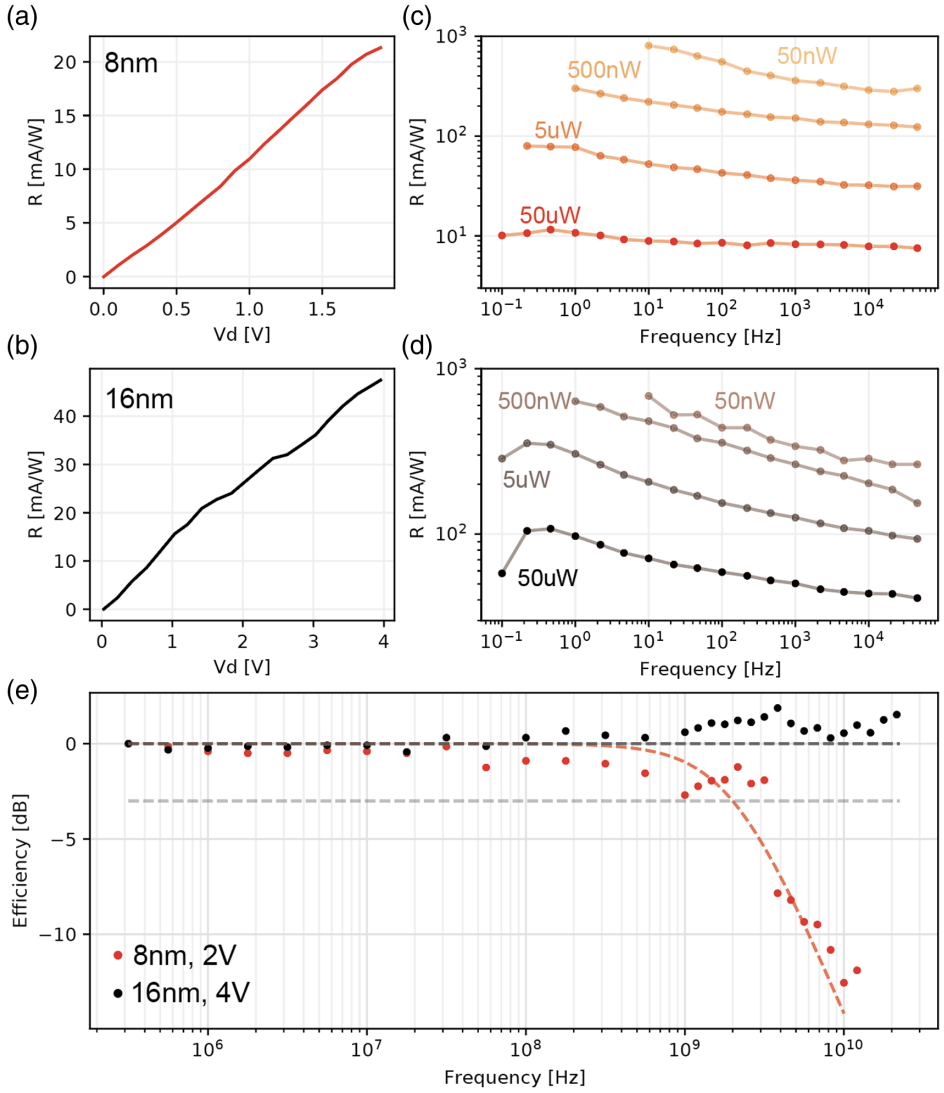

Fig. 3. Telecom characterization. (a) Voltage-dependent responsivity of a 100 μm wide 8 nm thick Te device on silicon measured at 50 μW optical power and 50 MHz. (b) Voltage-dependent responsivity of a 20 μm wide 16 nm thick Te measured at 150 μW optical power and 10 kHz. (c) Low-power low-frequency characterization of a 5 μm wide 8 nm thick Te device. (d) Low-power low-frequency characterization of a 20 μm wide 16 nm thick Te device. (e) High-speed measurements of 8 and 16 nm thick devices. 2 and 4 V are used for 8 and 16 nm speed measurements, respectively. Efficiency normalized to 6 mAW^{-1} for 8 nm devices and 11 mAW^{-1} for 16 nm devices, measured with 150 μW input power. All measurements are at 1546 nm. The gray dotted line indicates −3 dB.

different performance than immediately after fabrication. This is consistent with a previous report [19] showing the air stability of Te flakes.

Moreover, as we can fabricate these detectors directly on top of existing photonic structures owing to the ease of integration, we can co-design the photonics and detectors to optimize their performance. We demonstrate this co-design process by resonantly enhancing the absorption of a small-area photodetector with an integrated Fabry–Perot cavity, shown in Fig. 4(a). The cavity is designed to critically couple light from the waveguide to the Te photodetector for maximum absorption. This is achieved by matching the reflection of the input mirror to the calculated absorption of a small area of Te, which is then lithographically patterned on top. As these detectors are operating in photoconductive mode, the dark current can add significant noise. Therefore, shrinking the active area of the detector while maintaining a similar level of absorption increases the signal to noise ratio. To achieve this, we co-engineer the integrated photonic cavity and length of the deposited Te thin film that correspond to the absorption per an optical pass on the integrated cavity. Critically, the liftoff based definition process for Te thin film allows for precise control of the absorption per optical pass, and hence allows for better coupling to the integrated cavity. As shown in Fig. 4(b), we are able to resonantly enhance the absorption of a 1 μm wide device, achieving a peak responsivity of 8 mAW^{-1} with a dark current of 25 μA, compared to the 11 mAW^{-1} responsivity and 500 μA dark current of a 20 μm non-resonant device. This shows more than an order of magnitude reduction in dark current with a comparable responsivity. We note that the quality factor of the resonant device is approximately 500, which corresponds to 3 dB bandwidth of 370 GHz. Hence, this cavity integration would not compromise the device speed.

To demonstrate flexible integration and broadband operation of evaporated Te detectors, we integrate detectors onto silicon

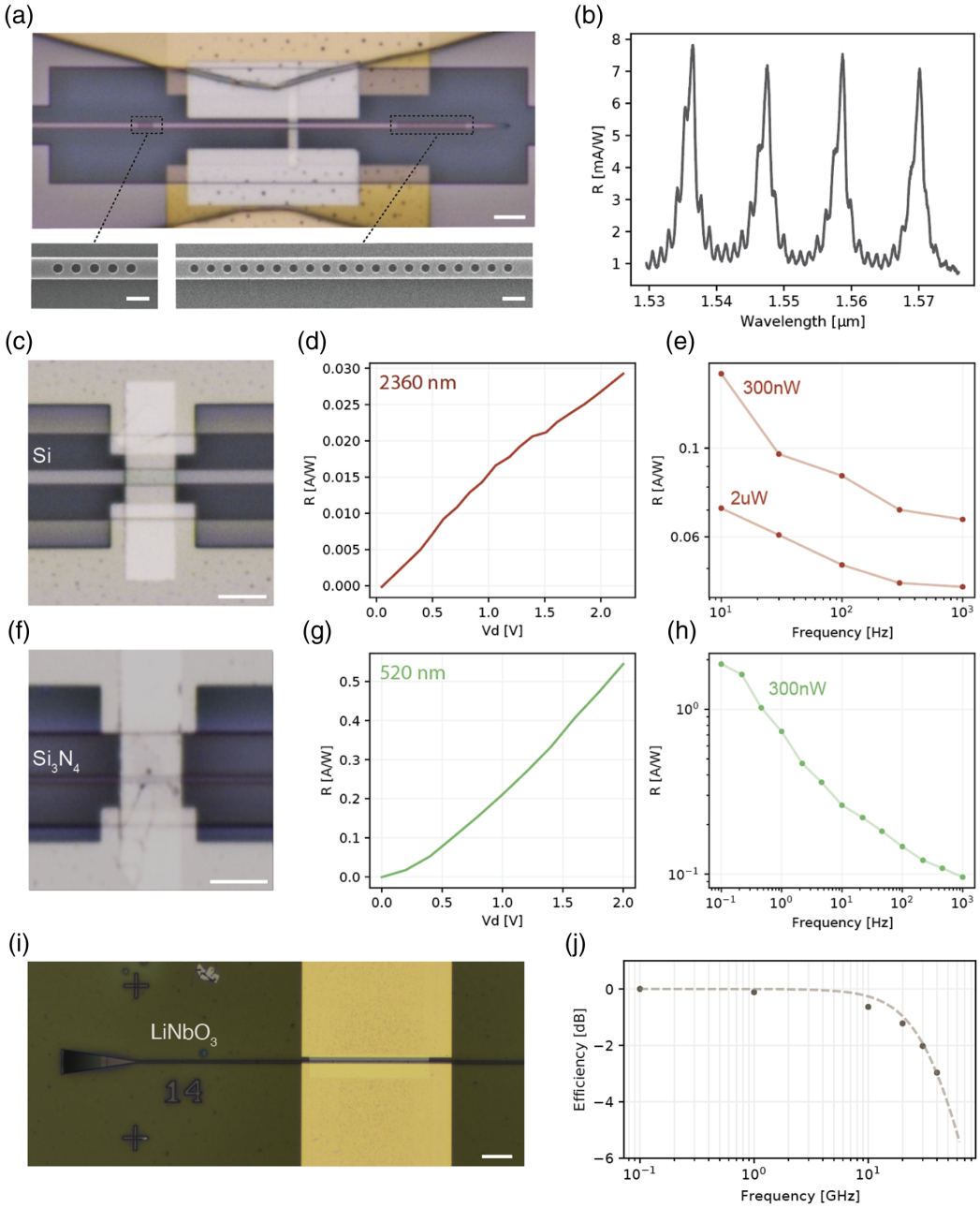

Fig. 4. Flexible integration. (a) Optical micrograph and SEMs of an integrated Fabry–Perot cavity in silicon that enhances a 1 μm wide 16 nm Te device absorption. Scale bars are 3 μm (top) and 500 nm (bottom). (b) Responsivity over wavelength of integrated Te-cavity device. Resonant enhancement shows more than half of the responsivity of a 20 μm long device with far less dark current. (c) Optical micrograph of a 16 nm thick device on silicon operating at 2360 nm (scale bar is 5 μm). (d) Voltage-dependent responsivity measured at 2 μW input power and 1 kHz. (e) Low-power, low-frequency response of the same device. (f) Optical micrograph of a 16 nm thick device on silicon nitride operating at 520 nm on a silicon nitride waveguide (scale bar is 5 μm). (g) Voltage-dependent responsivity measured at 2 μW input power and 1 kHz. (h) Low-power, low-frequency response of the same device. (i) Optical micrograph of thin-film lithium niobate on sapphire integration. Scale bar is 25 μm (j) Frequency-dependent responsivity of LN device showing operation up to 40 GHz. Measured with 100 μW input power at 1557 nm. Normalized to a responsivity of 17.5 mA/W. Dashed line shows a 3 dB bandwidth of 40 GHz.

devices operating in the mid-IR [Figs. 4(c)–4(e)] and onto silicon nitride devices operating in the visible range [Figs. 4(f)–4(h)]. In both devices, we again see enhanced responsivities at low power and low frequency. The silicon based device achieves a maximum responsivity of 0.15 AW^{-1} at 2360 nm. The visible device with silicon nitride photonics achieves a responsivity of 1.9 AW^{-1} at 520 nm. This indicates that waveguide integrated Te photodetectors can operate efficiently across a wide wavelength band and can operate with arbitrary photonic circuits underneath.

Finally, we fabricate detectors on thin-film lithium niobate devices designed for 1550 nm [Fig. 4(i)]. Using an external high-speed electro-optic modulator, we measure the RF-dependent responsivity [Fig. 4(j)]. We find that the 3 dB bandwidth is larger

than but likely close to 40 GHz. From this measurement, we can get a more accurate estimation for the carrier mobility of 486 $cm^2V^{-1}s^{-1}$ (40 GHz bandwidth with a 2.7 μm gap and a 3 V bias). Given this high mobility present in Te films, by shrinking l to 1×10^{-6} m, which is still easily achieved with scalable photolithography, these photodetectors can potentially reach operation bandwidths close to 300 GHz. The RC bandwidth from the contact capacitance and resistance (measured contact resistance of 200Ω and calculated 2 fF capacitance) is approximately 400 GHz, so the operation would not be RC bandwidth limited.

3. CONCLUSION

We demonstrated air-stable evaporated Te photodiodes that are easy to fabricate, can achieve high efficiency, and can be flexibly integrated onto numerous photonics platforms for wavelengths ranging from visible to mid-IR. Our thermal evaporation of Te thin films leaves the Te crystalline with extremely high carrier mobility, allowing us to demonstrate state-of-the-art detection bandwidths above 40 GHz, with beyond 100 GHz bandwidths easily achievable. We believe that improvements in the film quality of evaporated Te can further enhance the performance of Te photodetectors. These integrated Te devices will functionalize the on-chip detection of light in many material systems that lacked integrated photodetection, opening up these platforms for novel applications and widespread deployment. For instance, the integration of high-speed photodetectors on lithium niobate can enable single-chip photonic systems that take advantage of high-speed electro-optic modulators [32] for communication and frequency modulated continuous wave (FMCW) LiDAR. The integration of high-efficiency photodetectors on flexible substrates can enable more complex and compact optical biosensors [33], and scalable integration of photodetectors operating at mid-IR can enable on-chip mid-IR spectrometers for environment sensing and pollution monitoring. Additionally, evaporated Te has shown promise for high-performance field-effect transistors, which in combination with their photo-detectivity opens up a large space for photonic–electronic co-integration for complex systems beyond silicon photonics.

Funding. U.S. Department of Energy (DE-AC02-05-CH11231 (EMAT program KC1201), DE-AC02-76SF00515, FWP 100786); Defense Advanced Research Projects Agency (LUMOS); Kwanjeong Educational Foundation; National Science Foundation Graduate Research Fellowship Program (DGE-1656518); Natural Sciences and Engineering Research Council of Canada (NSERC); Defense Advanced Research Projects Agency (DARPA); SLAC National Accelerator Laboratory.

Acknowledgment. The authors thank Melissa Guidry and Kasper Van Gasse for assistance with the experimental setup, and Rahul Trivedi and David A.B. Miller for insightful discussions. G.H.A. acknowledges support from STMicroelectronics Stanford Graduate Fellowship (SGF) and Kwanjeong Educational Foundation. A.W. acknowledges the Herb and Jane Dwight Stanford Graduate Fellowship (SGF) and the NTT Research Fellowship. H.K. acknowledges support from Samsung Advanced Institute of Technology for part of this research conducted at Yonsei University. J.F.H. acknowledges support from the National Science Foundation Graduate Research Fellowship Program. K.K.S.M gratefully acknowledges support from the NSERC. Authors from Stanford acknowledge funding support from DARPA under the LUMOS program. The work at Stanford was supported by the Department of Energy, Atoms-to-Systems Co-Design: Transforming Data Flow to Accelerate Scientific Discovery project at SLAC National Accelerator Laboratory. The work at Berkeley was funded by the U.S. Department of Energy, Office of Science, Office of Basic Energy Sciences, Materials Sciences and Engineering Division.

Disclosures. The authors declare no conflicts of interest.

Data availability. Data underlying the results presented in this paper are not publicly available at this time but may be obtained from the authors upon reasonable request.

Supplemental document. See Supplement 1 for supporting content.

†These authors contributed equally to this paper.

REFERENCES

1. Y. Okawachi, K. Saha, J. S. Levy, Y. H. Wen, M. Lipson, and A. L. Gaeta, "Octave-spanning frequency comb generation in a silicon nitride chip," Opt. Lett. **36**, 3398–3400 (2011).
2. H. Jung, S.-P. Yu, D. R. Carlson, T. E. Drake, T. C. Briles, and S. B. Papp, "Tantala Kerr nonlinear integrated photonics," Optica **8**, 811–817 (2021).
3. J. Mishra, T. P. McKenna, E. Ng, H. S. Stokowski, M. Jankowski, C. Langrock, D. Heydari, H. Mabuchi, M. Fejer, and A. H. Safavi-Naeini, "Mid-infrared nonlinear optics in thin-film lithium niobate on sapphire," Optica **8**, 921–924 (2021).
4. D. M. Lukin, C. Dory, M. A. Guidry, K. Y. Yang, S. D. Mishra, R. Trivedi, M. Radulaski, S. Sun, D. Vercruysse, G. H. Ahn, and J. Vuckovic, "4h-silicon-carbide-on-insulator for integrated quantum and nonlinear photonics," Nat. Photonics **14**, 330–334 (2020).
5. C. Dory, D. Vercruysse, K. Y. Yang, N. V. Sapra, A. E. Rugar, S. Sun, D. M. Lukin, A. Y. Piggott, J. L. Zhang, M. Radulaski, K. G. Lagoudakis, L. Su, and J. Vuckovic, "Inverse-designed diamond photonics," Nat. Commun. **10**, 3309 (2019).
6. J. G. Bartholomew, J. Rochman, T. Xie, J. M. Kindem, A. Ruskuc, I. Craiciu, M. Lei, and A. Faraon, "On-chip coherent microwave-to-optical transduction mediated by ytterbium in YVO_4," Nat. Commun. **11**, 3266 (2020).
7. A. H. Atabaki, S. Moazeni, F. Pavanello, H. Gevorgyan, J. Notaros, L. Alloatti, M. T. Wade, C. Sun, S. A. Kruger, H. Meng, K. Al Qubaisi, I. Wang, B. Zhang, A. Khilo, C. V. Baiocco, M. Popović, V. M. Stojanović, and R. J. Ram, "Integrating photonics with silicon nanoelectronics for the next generation of systems on a chip," Nature **556**, 349–354 (2018).
8. C. Rogers, A. Y. Piggott, D. J. Thomson, R. F. Wiser, I. E. Opris, S. A. Fortune, A. J. Compston, A. Gondarenko, F. Meng, X. Chen, G. T. Reed, and R. Nicolaescu, "A universal 3D imaging sensor on a silicon photonics platform," Nature **590**, 256–261 (2021).
9. J. Michel, J. Liu, and L. C. Kimerling, "High-performance Ge-on-Si photodetectors," Nat. Photonics **4**, 527–534 (2010).
10. D. Liang, G. Roelkens, R. Baets, and J. E. Bowers, "Hybrid integrated platforms for silicon photonics," Materials **3**, 1782–1802 (2010).
11. A. Beling, A. S. Cross, M. Piels, J. Peters, Q. Zhou, J. E. Bowers, and J. C. Campbell, "Inp-based waveguide photodiodes heterogeneously integrated on silicon-on-insulator for photonic microwave generation," Opt. Express **21**, 25901–25906 (2013).
12. Y. Salamin, P. Ma, B. Baeuerle, A. Emboras, Y. Fedoryshyn, W. Heni, B. Cheng, A. Josten, and J. Leuthold, "100 GHz plasmonic photodetector," ACS Photon. **5**, 3291–3297 (2018).
13. Y. Liu, N. O. Weiss, X. Duan, H.-C. Cheng, Y. Huang, and X. Duan, "Van der Waals heterostructures and devices," Nat. Rev. Mater. **1**, 16042 (2016).
14. K. F. Mak and J. Shan, "Photonics and optoelectronics of 2D semiconductor transition metal dichalcogenides," Nat. Photonics **10**, 216–226 (2016).
15. N. Youngblood, C. Chen, S. J. Koester, and M. Li, "Waveguide-integrated black phosphorus photodetector with high responsivity and low dark current," Nat. Photonics **9**, 247–252 (2015).
16. R. Maiti, C. Patil, M. Saadi, T. Xie, J. Azadani, B. Uluutku, R. Amin, A. Briggs, M. Miscuglio, D. Van Thourhout, S. D. Solares, T. Low, R. Agarwal, S. R. Bank, and V. J. Sorger, "Strain-engineered high-responsivity mote 2 photodetector for silicon photonic integrated circuits," Nat. Photonics **14**, 578–584 (2020).
17. N. Flöry, P. Ma, Y. Salamin, A. Emboras, T. Taniguchi, K. Watanabe, J. Leuthold, and L. Novotny, "Waveguide-integrated van der waals heterostructure photodetector at telecom wavelengths with high speed and high responsivity," Nat. Nanotechnol. **15**, 118–124 (2020).

18. M. Amani, C. Tan, G. Zhang, C. Zhao, J. Bullock, X. Song, H. Kim, V. R. Shrestha, Y. Gao, K. B. Crozier, M. Scott, and A. Javey, "Solution-synthesized high-mobility tellurium nanoflakes for short-wave infrared photodetectors," ACS Nano **12**, 7253–7263 (2018).
19. L. Tong, X. Huang, P. Wang, L. Ye, M. Peng, L. An, Q. Sun, Y. Zhang, G. Yang, Z. Li, F. Zhong, F. Wang, Y. Wang, M. Motlag, W. Wu, G. J. Cheng, and W. Hu, "Stable mid-infrared polarization imaging based on quasi-2D tellurium at room temperature," Nat. Commun. **11**, 1–10 (2020).
20. A. Castellanos-Gomez, M. Buscema, R. Molenaar, V. Singh, L. Janssen, H. S. Van Der Zant, and G. A. Steele, "Deterministic transfer of two-dimensional materials by all-dry viscoelastic stamping," 2D Mater. **1**, 011002 (2014).
21. S. Marconi, M. Giambra, A. Montanaro, V. Mišeikis, S. Soresi, S. Tirelli, P. Galli, F. Buchali, W. Templ, C. Coletti, V. Sorianello, and M. Romagnoli, "Photo thermal effect graphene detector featuring 105 Gbits^{-1} NRZ and 120 Gbits^{-1} PAM4 direct detection," Nat. Commun. **12**, 806 (2021).
22. C. Liu, J. Guo, L. Yu, J. Li, M. Zhang, H. Li, Y. Shi, and D. Dai, "Silicon/2d-material photodetectors: from near-infrared to mid-infrared," Light Sci. Appl. **10**, 1–21 (2021).
23. M. Long, P. Wang, H. Fang, and W. Hu, "Progress, challenges, and opportunities for 2D material based photodetectors," Adv. Funct. Mater **29**, 1803807 (2019).
24. B. Chen, H. Sahin, A. Suslu, L. Ding, M. I. Bertoni, F. Peeters, and S. Tongay, "Environmental changes in mote2 excitonic dynamics by defects-activated molecular interaction," ACS Nano **9**, 5326–5332 (2015).
25. K. Kang, S. Xie, L. Huang, Y. Han, P. Y. Huang, K. F. Mak, C.-J. Kim, D. Muller, and J. Park, "High-mobility three-atom-thick semiconducting films with wafer-scale homogeneity," Nature **520**, 656–660 (2015).
26. C. Zhao, C. Tan, D.-H. Lien, X. Song, M. Amani, M. Hettick, H. Y. Y. Nyein, Z. Yuan, L. Li, M. C. Scott, and A. Javey, "Evaporated tellurium thin films for p-type field-effect transistors and circuits," Nat. Nanotechnol. **15**, 53–58 (2020).
27. C. Zhao, H. Batiz, B. Yasar, H. Kim, W. Ji, M. C. Scott, D. C. Chrzan, and A. Javey, "Tellurium single-crystal arrays by low-temperature evaporation and crystallization," Adv. Mater. **33**, 2100860 (2021).
28. C. Tan, M. Amani, C. Zhao, M. Hettick, X. Song, D.-H. Lien, H. Li, M. Yeh, V. R. Shrestha, K. B. Crozier, M. C. Scott, and A. Javey, "Evaporated sexte1-x thin films with tunable bandgaps for short-wave infrared photodetectors," Adv. Mater. **32**, 2001329 (2020).
29. G. Qiu, S. Huang, M. Segovia, P. K. Venuthurumilli, Y. Wang, W. Wu, X. Xu, and P. D. Ye, "Thermoelectric performance of 2D tellurium with accumulation contacts," Nano Lett. **19**, 1955–1962 (2019).
30. Y. Fang, A. Armin, P. Meredith, and J. Huang, "Accurate characterization of next-generation thin-film photodetectors," Nat. Photonics **13**, 1–4 (2019).
31. Y. Dan, X. Zhao, K. Chen, and A. Mesli, "A photoconductor intrinsically has no gain," ACS Photon. **5**, 4111–4116 (2018).
32. C. Wang, M. Zhang, X. Chen, M. Bertrand, A. Shams-Ansari, S. Chandrasekhar, P. Winzer, and M. Lončar, "Integrated lithium niobate electro-optic modulators operating at CMOS-compatible voltages," Nature **562**, 101–104 (2018).
33. L. Li, H. Lin, S. Qiao, Y.-Z. Huang, J.-Y. Li, J. Michon, T. Gu, C. Alosno-Ramos, L. Vivien, A. Yadav, K. Richardson, N. Lu, and J. Hu, "Monolithically integrated stretchable photonics," Light Sci. Appl. **7**, 17138 (2018).